

Irradiation effects on Al_{0.3}CoCrFeNi and CoCrMnFeNi high-entropy alloys, and 316H stainless steel at 500 °C

Wei-Ying Chen ^{a,*}, Marquis A. Kirk ^a, Naoyuki Hashimoto ^b, Jien-Wei Yeh ^c, Xiang Liu ^d, Yiren Chen ^a

^a Argonne National Laboratory, Lemont, IL, USA

^b Hokkaido University, Sapporo, Japan

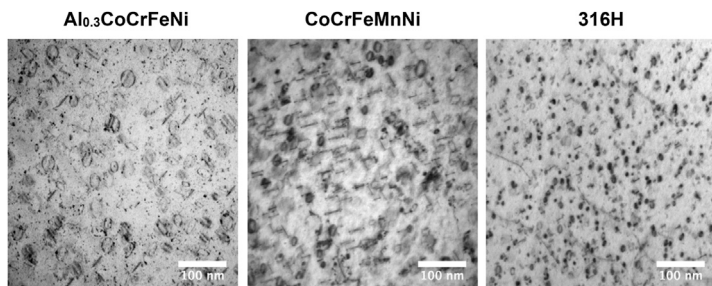
^c National Tsing Hua University, Hsing-Chu, Taiwan

^d Idaho National Laboratory, Idaho Falls, ID, USA



GRAPHICAL ABSTRACT

Bright-field TEM micrographs of Al_{0.3}CoCrFeNi, CoCrFeMnNi and 316H SS irradiated with 1 MeV Kr ions at 500 °C to 1 dpa. All images were taken at similar foil thickness near 110 zone axis with g = 200. The two high entropy alloys exhibited significantly larger size and smaller density of dislocation loops as compared with the 316H stainless steels.



ARTICLE INFO

Article history:

Received 28 January 2020

Received in revised form

27 May 2020

Accepted 10 June 2020

Available online 12 June 2020

ABSTRACT

To evaluate the potential of high entropy alloys (HEAs) for nuclear applications, two HEAs, Al_{0.3}CoCrFeNi and CoCrFeMnNi, and a conventional Type 316H stainless steel (SS) were irradiated with 1 MeV krypton ions at 500 °C up to 1 dpa, and examined *in-situ* with a transmission electron microscope (TEM). After irradiation, a high density of ordered L₁₂ nanoparticles was observed in Al_{0.3}CoCrFeNi. In contrast, no phase transformation was observed in CoCrFeMnNi and 316H SS. In the thin foil regions of TEM samples, stacking-fault tetrahedra were observed in the HEAs. In the thick foil regions, interstitial dislocation loops were observed for all alloys, and the areal loop density increased linearly with foil thickness. The Al_{0.3}CoCrFeNi had the largest loop size (the lowest density), followed by the CoCrFeMnNi and then the 316H SS. The higher loop nucleation rate in the 316H SS was attributed to carbon content. The degree of irradiation hardening was slightly lower for the HEAs than for the 316H SS, which is a promising sign for the nuclear application of HEAs at high temperatures.

Published by Elsevier B.V.

1. Introduction

Recently, high-entropy alloys (HEAs) have attracted great attention in the nuclear materials community because of their

* Corresponding author.

E-mail address: wychen@anl.gov (W.-Y. Chen).

high-temperature strength and radiation resistance [1–10]. HEAs are an alloy system composed of five or more principle elements in near equimolar ratios. These novel alloys have much higher configurational entropy than that of traditional alloys and can enhance their phase stability at high temperatures. The distorted lattice and sluggish diffusion in HEAs can immobilize radiation-induced point defects, leading to a high level of radiation resistance [11]. Indeed, HEAs have shown lower degrees of irradiation swelling [6,8] and radiation-induced segregation [1] as compared with traditional materials with less alloying complexity.

Despite these promising results, the irradiation-induced hardening and embrittlement of HEAs are not well understood. Irradiation-induced dislocation loops are a key contributor to the irradiation hardening and embrittlement of materials. A quantitative analysis of the irradiation-induced dislocation loops as a function of irradiation conditions (dose, dose rate, temperature etc.) and compositions is crucial for improving our understanding on the mechanical property degradation of HEAs under irradiation.

Recent studies that attempt to correlate the production of dislocation loops and the compositional complexity of HEAs showed mixed results. For example, Lu et al. reported that the loop size decreased and the loop density increased with the increasing compositional complexity of alloys (Ni, NiCo, NiFe, NiCoFe, Ni-CoFeCr and NiCoFeCrMn) under 1.5–3 MeV nickel ion irradiation at 500 °C to 4–60 dpa [5,6]. However, with the same set of alloys, Shi et al. observed an opposite behavior under *in-situ* 1 MeV krypton ion irradiation at 500 °C to 2 dpa [12]. The loop size increased, and the loop density decreased with the increasing compositional complexity. These conflicting results indicate that the formation and growth of irradiation-induced dislocation loops in HEAs require further research.

Furthermore, as a new class of materials, most initial research has been focusing on contrasting HEAs with pure metals and model alloys [5,6,8,12–14]. To move forward with real-world applications, it is important to demonstrate the advantages of HEAs over common commercial alloys. Currently, only a couple of studies are recently published to compare HEAs directly with commercial alloys for their irradiation performance [1,15]. Kumar et al. irradiated a FeNiMnCr HEA with 3 and 5.8 MeV nickel ions up to 10 dpa from room temperature to 700 °C, and compared the results with austenitic stainless steels (SS) [1]. They found that the loop morphology in the HEA and austenitic SS was comparable below 400 °C. When the irradiation temperature was above 400 °C, the loop density was higher, but the loop size was lower, in the HEA than those in the austenitic SS. Our previous work on an *in-situ* 1 MeV krypton ion irradiation showed that the loop evolution and corresponding hardening were comparable for two HEAs (Al_{0.3}CoCrFeNi and CoCrFeMnNi) and a 316H SS at 300 °C up to 1 dpa [15]. Since the diffusion and effect of configurational entropy is a strong function of temperature, the defect evolution in HEAs is expected to be different at high temperatures. The benefit of alloying complexity affecting the evolution of dislocation loops might be more effective at temperatures higher than 300 °C.

In addition, the phase stability of HEAs under irradiation needs to be studied. In concept, the high configuration entropy and sluggish diffusion can stabilize the HEAs in a single-phase solid solution at high temperatures. In practice, the formation of intermetallics can still occur at the operating temperatures of advanced nuclear reactors (e.g. 400–700 °C for sodium fast reactors and molten salt reactors [16]). As reported by Kumar et al. [1], a FeNiMnCr HEA remained as single phase after irradiation at room temperature to 700 °C up to 10 dpa. On the other hand, our previous study indicated that the Al_{0.3}CoCrFeNi HEA experienced some ordering after irradiation at 300 °C to 1 dpa [15]. It is important to investigate the phase stability of HEAs under irradiation, and

compare with conventional alloys such as 316 SS.

In the present study, we compared the microstructural evolution of two fcc HEAs and austenitic SS under irradiation at 500 °C. The defect morphology and phase stability were evaluated, and the core effects of the novel qualities of HEAs (i.e., high entropy, severe lattice distortion, sluggish diffusion and cocktail [17]) on radiation resistance were investigated.

2. Materials and experiments

Two fcc HEAs, CoCrFeMnNi and Al_{0.3}CoCrFeNi, and a Type 316H SS were included in this study. These alloys are identical to those used in our previous study at 300 °C [15]. The CoCrFeMnNi and Al_{0.3}CoCrFeNi were fabricated at National Tsing Hua University by arc-melting. The obtained HEAs were cold rolled up to 70%, homogenized at 1200 °C for 48 h, and then water quenched. The 316H SS was solution annealed at 1065 °C for 1 h, followed by water quench. The compositions of these alloys are given in Table 1.

The inclusions, grain sizes and dislocation densities of the as received HEAs and 316H SS are given in Table 2. Three-millimeter diameter transmission electron microscopy (TEM) disks for *in-situ* ion irradiation experiments were prepared by mechanical thinning followed by electro-polishing. The polishing was performed with an electrolyte of 5% perchloric acid and 95% methanol at –40 °C with a Struers TenuPol-5 jet polisher.

The TEM specimens were irradiated with 1 MeV krypton ions at 500 °C to a fluence of 6.3×10^{14} ions·cm⁻² inside a Hitachi-9000 TEM in the Intermediate-Voltage Electron Microscopy (IVEM)-Tandem facility at Argonne National Laboratory. The ion flux was about 1.3×10^{12} ions·cm⁻²·s⁻¹ in the irradiation experiments. The microscope was operated at 300 kV. The profile of irradiation damage was calculated with the Stopping and Range of Ions in Matter (SRIM) with the quick Kinchin-Pease option [18] for each material as shown in Fig. 1. The displacement dose at 100 nm below the irradiation surface on the SRIM profile was used as the nominal dose for each irradiation experiment.

The irradiation-induced defects in HEAs and 316H SS were consistently recorded with kinematic bright field and weak-beam dark field (WBDF) TEM images using $g = (200)$ at [011] zone axis as a function of dose from 1.9×10^{13} to 6.3×10^{14} ions·cm⁻². The size of dislocation loops was measured for all doses. The loop density was determined at the end dose, 6.3×10^{14} ions·cm⁻², by measuring the defect areal density as a function of foil thickness in order to account for the surface sink effect [19]. The foil thickness was estimated by thickness fringes. In addition, the same-area TEM images were taken with $g = (001)$, $(0\bar{2}\bar{2})$ and (022) at [100] zone axis for investigating the Burgers vector of dislocation loops in 316H SS.

To evaluate irradiation hardening, nanoindentation experiments were performed on another set of samples irradiated *ex-situ* at the IVEM-Tandem facility. The specimens were mechanically polished with abrasive papers and diamond suspension down to 1 μm. Subsequently, the specimens were electropolished for 20 s with the same electrolyte used for the TEM sample preparation. After the polishing, the specimens were irradiated on a temperature-controlled stage with the same irradiation conditions used in the *in-situ* experiments.

Table 1

Material compositions (at%).

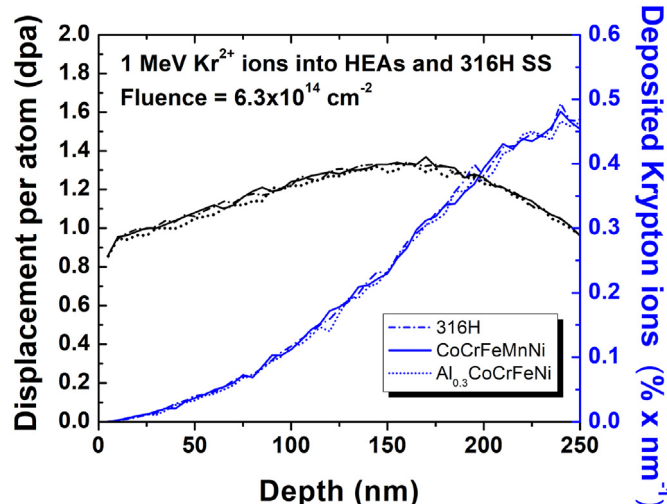
	Fe	Cr	Ni	Mn	Co	Al	Mo	Si	C	N
Al _{0.3} CoCrFeNi ^a	23.3	23.3	23.3		23.3	6.8				
CoCrFeMnNi ^a	20	20	20	20	20					
316H ^{a,b}	bal.	18.4	12.5	2.1			1.4	1.2	0.3	0.1

^a Nominal.

^b 316H also contains 0.03% P, 0.03% S and <0.01% B.

Table 2Microstructural parameters and microhardness of as received and irradiated specimens^b.

	Al _{0.3} CoCrFeNi	CoCrMnFeNi	316H SS	
Pre-irradiation characterization				
Grain size (μm)	~500	~400	~100	
Dislocation density (m^{-2})	$\sim 10^{12}$	$\sim 10^{12}$	$\sim 10^{12}$	
Inclusion volume fraction (%)	0.08	0.45	0.18	
Hardness as received H_0 (GPa) ^a	3.56 ± 0.05	3.14 ± 0.09	2.97 ± 0.04	
Post-irradiation characterization				
Dislocation Loop density (m^{-3})	300 °C 500 °C	1.3×10^{23} 5.2×10^{21}	1.2×10^{23} 9.7×10^{21}	7.5×10^{22} 2.3×10^{22}
Dislocation Loop Size (nm)	300 °C 500 °C	2.8 23.9	2.7 19.2	3.3 9.9
$1/3<111>$ loops: $1/2<110>$ loops	500 °C	73.7%: 26.3%	73.5%: 26.5%	Predominantly $1/3<111>$ loops
Hardness After 1 dpa irradiation H_{irr} (GPa) ^a	300 °C 500 °C	4.63 ± 0.03 4.21 ± 0.02	4.37 ± 0.12 3.92 ± 0.09	3.98 ± 0.06 3.77 ± 0.05
$\Delta H = H_{\text{irr}} - H_0$ (GPa)	300 °C 500 °C	1.07 ± 0.06 0.65 ± 0.05	1.23 ± 0.15 0.78 ± 0.12	1.01 ± 0.07 0.80 ± 0.07
$\Delta\sigma_{y,c}$ (GPa)	300 °C 500 °C	1.37 0.81	1.27 0.93	1.14 1.10

^a The uncertainty of the measured hardness equals one standard deviation of the hardness data.^b Data for the as received and 300 °C irradiation was from Ref. [15].**Fig. 1.** SRIM calculations of the displacement damage and distributions of 1 MeV krypton ions in 316H SS, CoCrFeMnNi and Al_{0.3}CoCrFeNi.

Before nanoindentation, the specimens were superglued on magnetic disks and dried for at least 5 h. The nanoindentation was performed at the University of Illinois at Urbana-Champaign with a Hysitron TI 950 Triboindenter. A Berkovich tip was used in these tests and the indenter was operated in a quasi-static mode with a nominal displacement of 100 nm. As shown by Hosemann et al. [20], the results of nanoindentation on ion-irradiated materials are affected by indentation size and the soft unirradiated substrate. It was suggested that the plastic zone of a typical Berkovich tip is about 5 times the indentation depth. Therefore, as described in our previous work [15], the indentation condition of a fixed displacement of 100 nm was specifically chosen in order to mitigate the effect of indentation size and the soft unirradiated substrate. At least 16 indents were carried out for each specimen.

3. Results

3.1. Phase stability

The phase stabilities of the HEAs and 316H SS were studied with *in-situ* irradiation. Before irradiation, the TEM diffraction patterns

of the as received HEAs and 316H SS all showed single-phase face-centered-cubic (fcc) crystal structures with no indication of ordered or secondary phases [15]. After irradiation at 500 °C to 1 dpa, extra diffraction spots were visible as shown in Fig. 2. These extra spots can be categorized into three types: (1) double diffraction from oxides epitaxially formed on the foil surface, (2) fcc forbidden reflections, and (3) possibly {1100} hcp reflections.

As indicated by the red arrows in Fig. 2, the double diffraction was observed around the primary reflections and the direct beam in all HEAs and 316H SS after irradiation at 500 °C. This double diffraction comes from the oxide layer on the surface of the TEM foils. The observed oxidation diffraction spots are similar to the observation by He et al. on CrFeCoNi-based alloys heated to 400 °C inside TEM [13]. As compared with the Al_{0.3}CoCrFeNi and 316H SS, the CoCrFeMnNi tends to have thicker surface oxidation, especially near the edge of the foil. In order to reduce the diffraction intensity from the surface oxide, the irradiated CoCrFeMnNi was gently cleaned with 0.3 keV argon ions at an angle of $\pm 5^\circ$ for 90 s, and then 0.1 keV for 30 s. This gentle cleaning process reduces the thickness of oxide layer but allowed some remaining oxides on the surface after milling, preserving the underneath material. For the Al_{0.3}CoCrFeNi and 316H, the double diffraction from surface oxides was not significant, and thus their diffraction patterns were taken without cleaning.

The fcc forbidden reflections, as indicated with yellow arrows, were observed in the Al_{0.3}CoCrFeNi only. The forbidden spots indicate the development of a long-range order in the irradiated Al_{0.3}CoCrFeNi as compared to the as received counterpart. The superlattice peaks are consistent with the L₁₂ ordered phase previously observed elsewhere in Al_xCoCrCuFeNi high entropy alloys [21], and in Al_{0.3}CoCrFeNi after 3 MeV Au ion irradiation at 500 °C [10]. As shown in Fig. 3, the dark-field image formed with a L₁₂ super lattice spot shows a high density of nanoscale L₁₂ particles with an average size of 1.1 nm and a density of several 10^{23} m^{-3} .

In order to separate the thermal and irradiation effects on the formation of L₁₂ phase, another Al_{0.3}CoCrFeNi sample was annealed in the TEM at 500 °C for 30 min without irradiation. This annealing time was about 3 times longer than the irradiation time. As shown in Fig. 2, the development of ordering resulting from thermal annealing is insignificant. This result suggests that the irradiation enhanced the formation of L₁₂ phase in Al_{0.3}CoCrFeN at 500 °C.

Finally, the {1100} hcp reflections, as indicated with the green arrows, were observed in the diffraction patterns of 111 zone for all

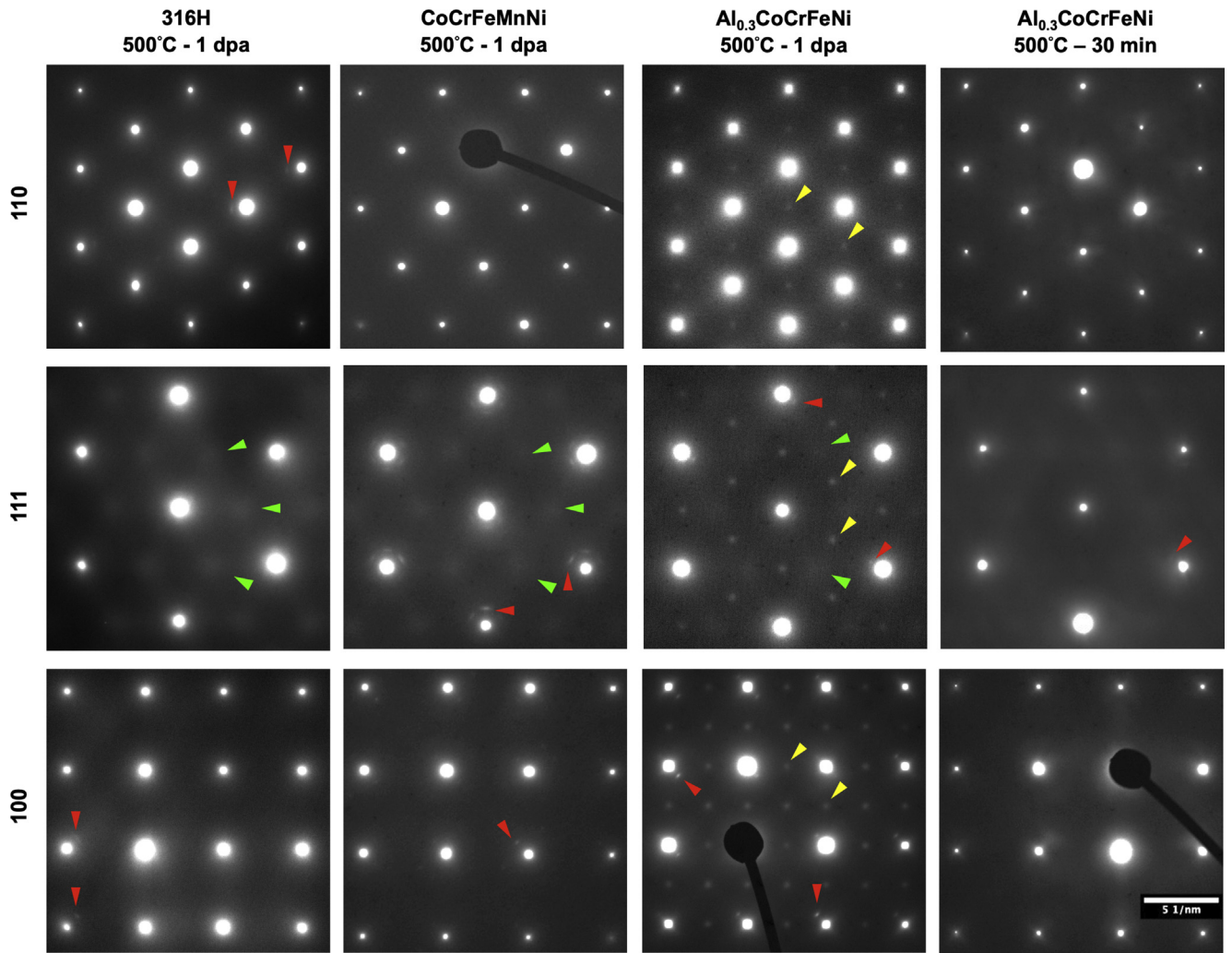


Fig. 2. The [110], [111], and [100] zone axis diffraction patterns of (column 1–3), 316H SS, CoCrFeMnNi and Al_{0.3}CoCrFeNi irradiated with 1 MeV krypton ions at 500 °C to 1 dpa, and (column 4) Al_{0.3}CoCrFeNi annealed at 500 °C for 30 min. The arrows indicate selected diffractions spots from ordered L1₂ phase (yellow), hcp reflections from the stacking faults (green), and double diffraction from the oxides formed on the foil surface (red). (For interpretation of the references to colour in this figure legend, the reader is referred to the Web version of this article.)

materials after irradiation. The hcp reflections were possibly resulted from the stacking faults of the irradiation-induced 1/3<111>{111} dislocation loops and the pre-existing Shockley partial dislocations, which are themselves thin hcp platelets/ribbons on {111} planes.

3.2. Defect microstructure

As shown in Fig. 4 and Fig. 5, small defect clusters and dislocation loops were observed in all three materials after irradiation. No voids were observed, which was likely due to the insufficient vacancy mobility and the relatively low irradiation dose. Since the thin foils examined under the microscope have a wedge shape, the size and density of defects directly observed on a TEM image can be affected by two factors. First, a TEM image is a 2-D projection of a 3-D microstructure in the foil. Therefore, the areal density of defect clusters is proportional to the foil thickness, provided that the defect clusters are uniformly distributed. Secondly, the foil surface is a sink for mobile defects, and can affect the concentration profile of irradiation-induced point defects. Consequently, both the nature and quantity of defect clusters resolvable under TEM can be affected by the foil thickness. So, a surface effect is expected for thin

samples like the ones used in this study.

To understand the microstructural evolution in thin foils, the surface effect needs to be analyzed as a function of foil thickness [19]. Fig. 4 shows three dark-field images of the studied materials taken at a foil thickness of ~80 nm. At this thickness, only small defect clusters were observed. For the Al_{0.3}CoCrFeNi and CoCrFeMnNi, a high portion of defect clusters can be recognized as stacking fault tetrahedra (SFT). The SFT in the Al_{0.3}CoCrFeNi are slightly larger and better defined as compared with those in the CoCrFeMnNi. For the 316H SS, only a few defect clusters are SFT, as indicated with the red arrows, while the other features don't have a well-defined shape and are likely dislocation loops. Moiré fringes due to surface oxides were observed in the CoCrFeMnNi. In contrast, the Moiré fringes were much less evident in the Al_{0.3}CoCrFeNi and 316H SS.

When the foil thickness is more than ~100 nm, large dislocation loops up to ~40 nm started to appear uniformly as shown in Fig. 5. Their sizes were abruptly larger than the “black-spot” defect clusters in the thinner regions. The areal density of dislocation loops increased with the foil thickness. For the Al_{0.3}CoCrFeNi, a significant amount of small defect clusters was still visible in the thicker region, resulting in a bimodal size distribution of defect clusters. For the CoCrFeMnNi and 316H SS, the bimodal distribution was not

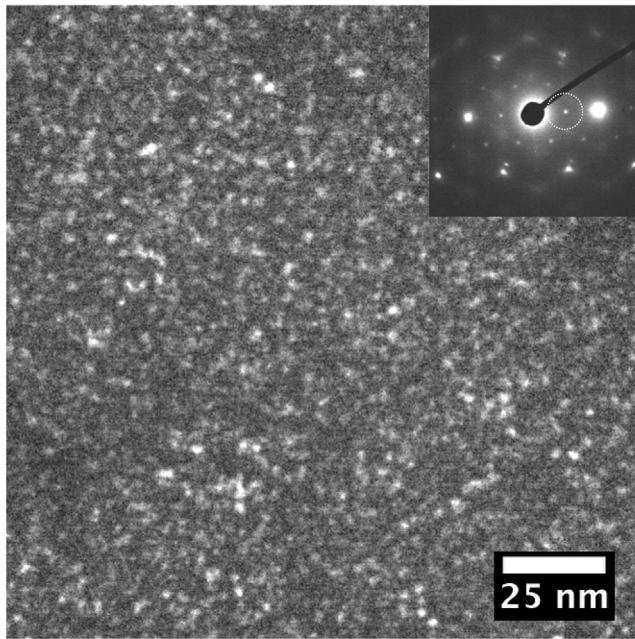


Fig. 3. Dark-field TEM image $\text{Al}_{0.3}\text{CoCrFeNi}$ irradiated at $500\text{ }^{\circ}\text{C}$ to 1 dpa. The image was formed with the L_2 superlattice spot circled with the dashed line in the inset SADP near [111] zone.

obvious. Up to about 250 nm in thickness, no dislocation networks were observed. No quantitative measurement was performed on the SFT and small defect clusters in the thicker regions because small defect clusters below ~ 2 nm are difficult to image in foils thicker than ~ 40 nm [22].

The size and density of large dislocation loops in 1 dpa samples as a function of foil thickness are shown in Fig. 6(a) and Fig. 6(b), respectively. For 316H SS, the loop sizes increase with the foil thickness below 150 nm, but become independent to the foil thickness above 150 nm. For HEAs, the thickness dependence between 100 nm and 150 nm is not obvious due to insignificant statistics. Fig. 6(c) shows the loop size as a function of dose where the measurement was performed on thicker regions of the foil (>150 nm). For all doses, the $\text{Al}_{0.3}\text{CoCrFeNi}$ and CoCrFeMnNi had evidently larger loop size as compared with 316H SS. Between $\text{Al}_{0.3}\text{CoCrFeNi}$ and CoCrFeMnNi, their loop size was indiscernible up

to 0.1 dpa. After that, however, the loop size in $\text{Al}_{0.3}\text{CoCrFeNi}$ was clearly larger than that in CoCrFeMnNi. Fig. 7 shows the loop size distributions for all samples at 1 dpa.

For each material, the loop volume density was calculated from the slope of its areal density versus foil thickness [19,22]. As shown in Fig. 6(b), the 316H SS has the highest loop density, followed by the CoCrFeMnNi and then the $\text{Al}_{0.3}\text{CoCrFeNi}$. The average size and density of dislocation loops are given in Table 2. The linear fitting lines for the data intercept the foil thickness axis at 95 nm, 91 nm, and 109 nm, respectively, for the $\text{Al}_{0.3}\text{CoCrFeNi}$, CoCrFeMnNi and 316H SS, respectively. A positive intercept on the thickness axis indicates a denuded zone for the large dislocation loops at foil surfaces. Assuming equal effects of both top and bottom surfaces, the HEAs and 316H SS had a denuded zone of about 50 nm for each side of the foil.

There are two types of dislocation loops in fcc alloys: faulted loops with Burgers vectors of $\mathbf{b} = 1/3<111>$, and perfect loops with the Burgers vector of $\mathbf{b} = 1/2<110>$. For the $\text{Al}_{0.3}\text{CoCrFeNi}$ and CoCrFeMnNi, the dislocation loops larger than 10 nm were used to determine their types with their shapes and stacking-fault fringes [6,10,12,13]. As shown in Fig. 5, the edge-on faulted $1/3[\bar{1}11]$ or $1/3[1\bar{1}1]$ loops are marked with red arrows, the inclined faulted $1/3[111]$ or $1/3[\bar{1}\bar{1}1]$ loops are marked with blue arrows, and the inclined perfect $1/2<110>$ loops are marked with green arrows. The ratios of $1/3<111>$ to $1/2<110>$ loops in HEAs are about 3:1 as shown in Table 2.

For the 316H SS, the loop size was not large enough for accurate determination of their types using [110] zone axis images, except for some edge-on faulted loops in Fig. 5. To determine the loop types in 316H SS, additional images at [100] zone axis with $\mathbf{g} = \pm(002)$, $\pm(022)$ and $\pm(0\bar{2}2)$ were obtained. Under this orientation, the perfect loops with $\mathbf{b} = 1/2[011]$ and $1/2[0\bar{1}1]$ would be imaged edge on. As shown in the first row of Fig. 8, when imaged with $\mathbf{g} = \pm 002$, two inclinations of dislocation loops were observed. The angle between the two inclinations was about 90° . When the same area was imaged with $\mathbf{g} = \pm(0\bar{2}2)$ (second row) or $\mathbf{g} = \pm(022)$, loops (third row), only one of the two inclinations were visible. This is consistent with that the loops in the second row were either $\mathbf{b} = 1/3[1\bar{1}1]$, $1/3[11\bar{1}]$ or $1/2[01\bar{1}]$, and $\mathbf{b} = 1/3[111]$, $1/3[\bar{1}\bar{1}1]$ or $1/2[011]$ for the third row, applying the $\mathbf{b} \cdot \mathbf{g}$ visibility criterion. To further differentiate the $1/2<110>$ and $1/3<111>$ loops, the shape of the loops in both inside and outside contrast were carefully examined, especially in the WBDF images. Under this crystal

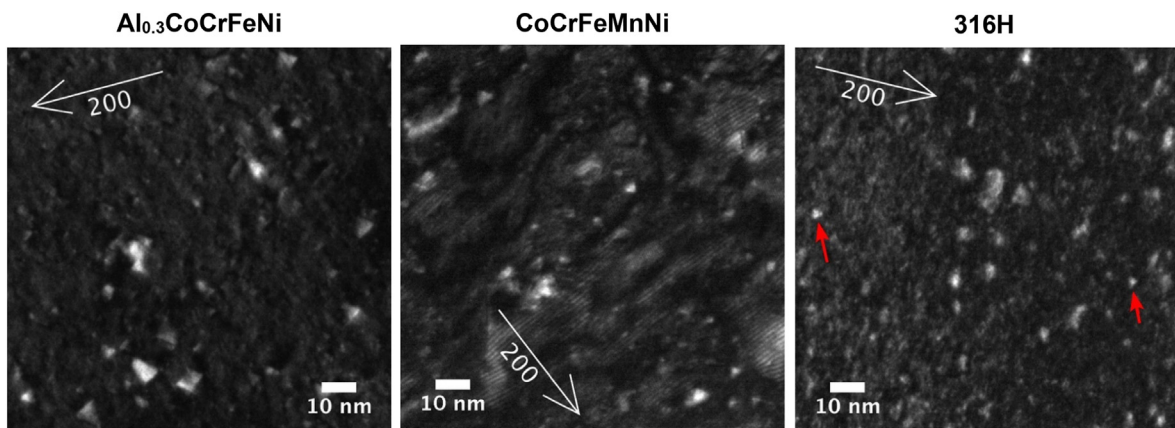


Fig. 4. Weak-beam dark field TEM images of $\text{Al}_{0.3}\text{CoCrFeNi}$, CoCrFeMnNi and 316H SS irradiated with 1 MeV Krypton ions at $500\text{ }^{\circ}\text{C}$ to 1 dpa. The images were taken at a foil thickness of 80 nm. The diffraction condition is $\mathbf{g} = 200$ ($\mathbf{g}, \mathbf{g}4\mathbf{g}$) at 011 zone. The red arrows indicate the SFT in 316H SS. The morié fringes in CoCrFeMnNi were oxides forming on the foil surface. (For interpretation of the references to colour in this figure legend, the reader is referred to the Web version of this article.)

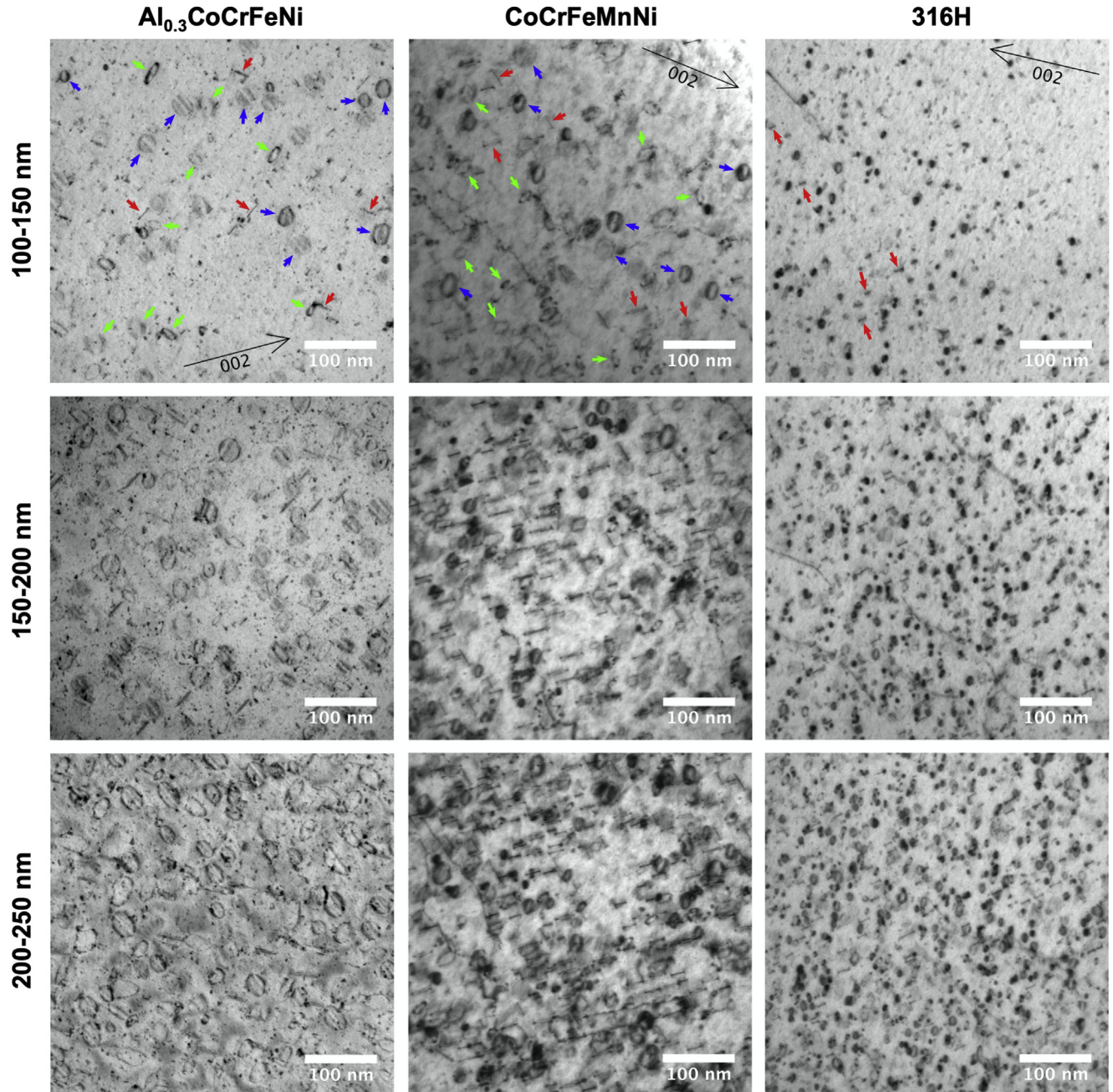


Fig. 5. Bright-field TEM images of $\text{Al}_{0.3}\text{CoCrFeNi}$, CoCrFeMnNi and 316H SS irradiated with 1 MeV Kr ions at 500 °C to 1 dpa as a function of foil thickness. All images were taken near 110 zone axis with $g = 200$.

orientation, all $1/3\bar{1}11$ faulted loops would be inclined with respect to the image plane. The $1/2[01\bar{1}]$ and $1/2[011]$ perfect loops, which comprise one third of the total population of perfect loops, would be edge on. As shown Fig. 8, the loops in 316H SS predominantly exhibited inside or outside contrast of inclined loops. No edge-on $1/2[011]$ and $1/2[\bar{0}11]$ perfect loops can be evidently observed. This indicates that faulted $1/3 < 111 >$ loops were predominant defects in the irradiated 316H SS.

3.3. Nanoindentation

The hardness measurements on the unirradiated and irradiated samples are shown in Table 2 and Fig. 9(a). The initial hardness of

both HEAs was higher than that of 316H SS. At 1 dpa, the hardness of all three materials increased at both irradiation temperatures of 300 °C and 500 °C. As shown in Fig. 9(b), the increases were more at 300 °C than at 500 °C. This indicates that a less degree of irradiation hardening was obtained at 500 °C. At 300 °C, the hardness increment ΔH for the 316H SS was less than that of the HEAs. In contrast, at 500 °C the hardness increment was higher for the 316H SS than for the HEAs. If we compare their relative hardening at 500 °C as shown in Fig. 9(c), the smaller hardening for HEAs as compared with 316H SS is even more obvious.

Since dislocation loops are the dominant defects for all materials in this study, the extent of irradiation hardening can be estimated with the quantitative measurements of dislocation loops. The

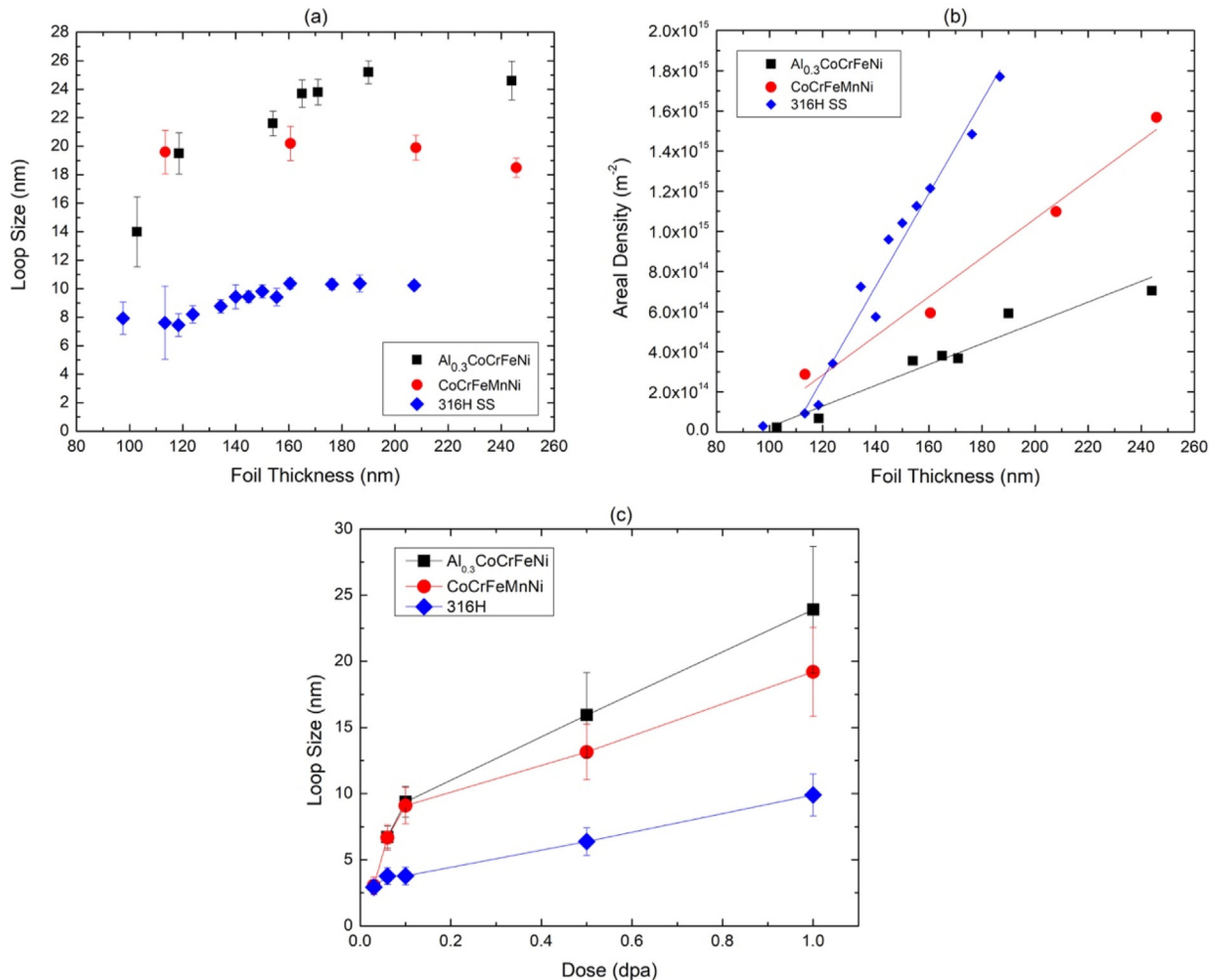


Fig. 6. (a) Size and (b) density of resolved dislocation loops as a function of specimen foil thickness for Al_{0.3}CoCrFeNi, CoCrFeMnNi and 316H SS irradiated with 1 MeV krypton ions at 500 °C to 1 dpa. (c) The average size of dislocation loops as a function of dose in the three materials.

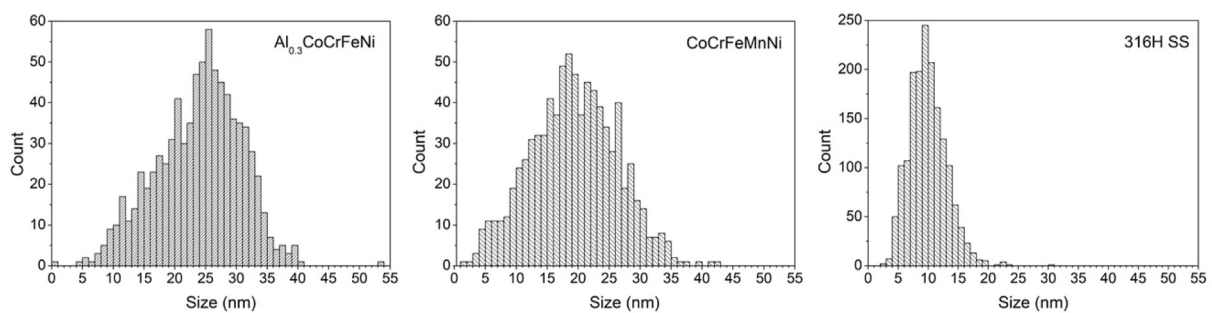


Fig. 7. The size distribution of resolved dislocation loops in Al_{0.3}CoCrFeNi, CoCrFeMnNi and 316H SS irradiated with 1 MeV krypton ions at 500 °C to 1 dpa.

increase in yield strength $\Delta\sigma_y$ due to irradiation-induced dislocation loops can be correlated with the Orowan hardening model:

$$\Delta\sigma_y = M\alpha\mu b\sqrt{Nd} \quad (1)$$

where M is the Taylor factor, α is the barrier strength factor of dislocation loops, μ is the shear modulus, b is the Burgers vector, and N and d are the density and size of dislocation loops, respectively. Fig. 9(d) shows the increases in yield strength calculated with Orowan equation (Eq. (1)) with the measured densities and

sizes of dislocation loops (Table 2). The parameters M , α , μ used in the calculations are 3.06, 0.4 and 77 GPa, respectively. The b is 0.257 nm for all materials. Note that a uniform size and density distribution of loops was assumed in the calculation. The effect of L1₂ particles, SFT and vacancy dislocation loops were ignored. Nevertheless, a consistent ranking among the three studied materials can be seen in Fig. 9(b) and (d) for the magnitude of irradiation hardening, which indicates that the irradiation hardening is dominated by the dislocation loops in the studied materials.

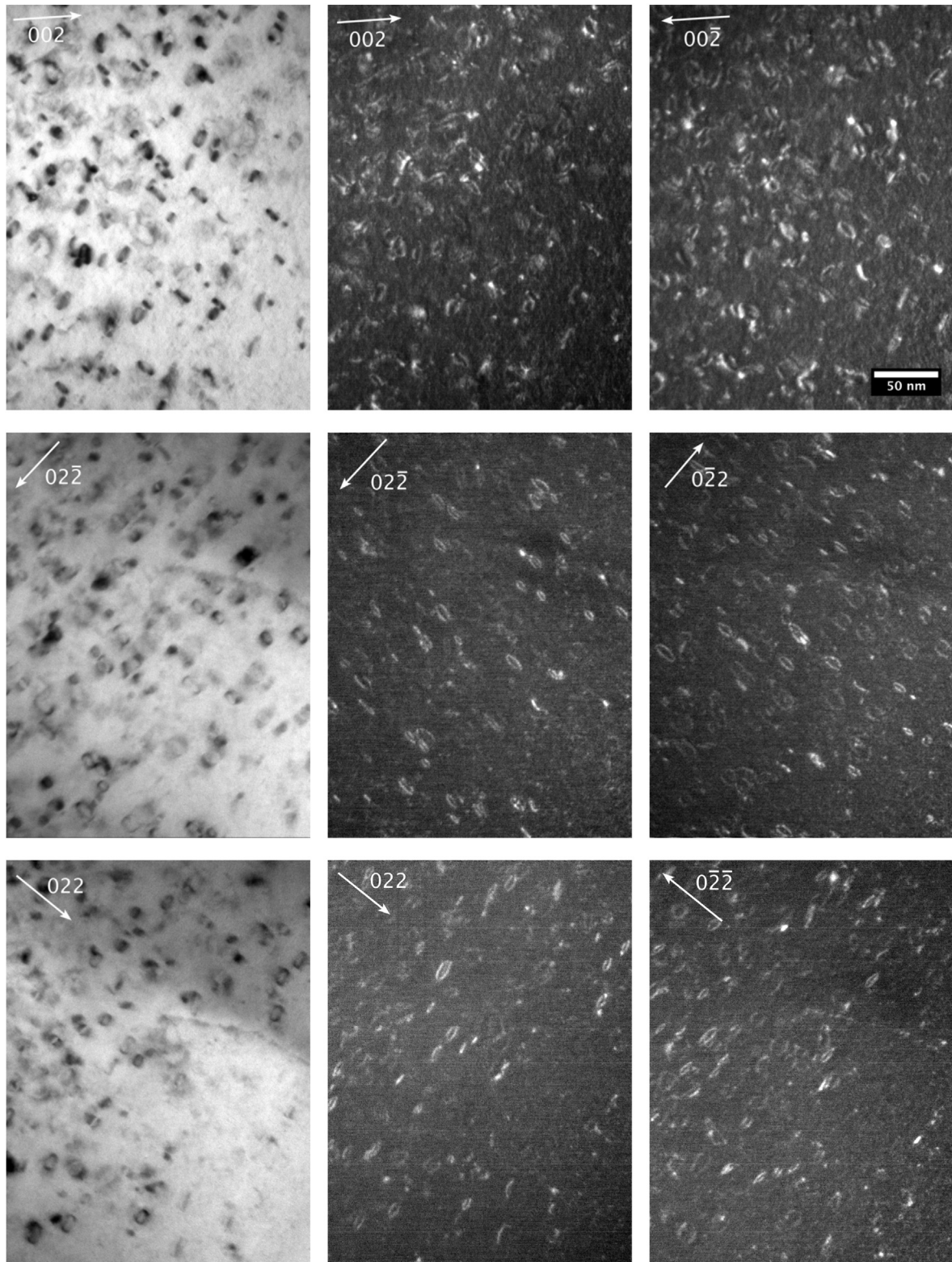


Fig. 8. Same area images of 316H SS irradiated with 1 MeV krypton ions at 500 °C to 1 dpa viewed at 100 zone axis with (1st row) $\mathbf{g} = \pm 002$, (2nd row) $\mathbf{g} = \pm 0\bar{2}2$, and $\mathbf{g} = \pm 022$. The left column is bright field images. The middle and right columns are WBDF images with the condition of $(\mathbf{g}, 4-5 \text{ g})$.

4. Discussion

4.1. Phase stability

In this study, the $\text{Al}_{0.3}\text{CoCrFeNi}$ was single-phase fcc in the

beginning. After irradiation at 500 °C to 1 dpa, homogeneous L1_2 nano-particles were observed. L1_2 is an ordered fcc intermetallic with a stoichiometry of Ni_3Al . Previously, L1_2 nano-particles have been found in as-cast $\text{Al}_x\text{CoCrCuFeNi}$ [21], as-cast [23] and 550°C-thermally-aged [24] $\text{Al}_{0.3}\text{CoCrFeNi}$, suggesting that L1_2 is stable

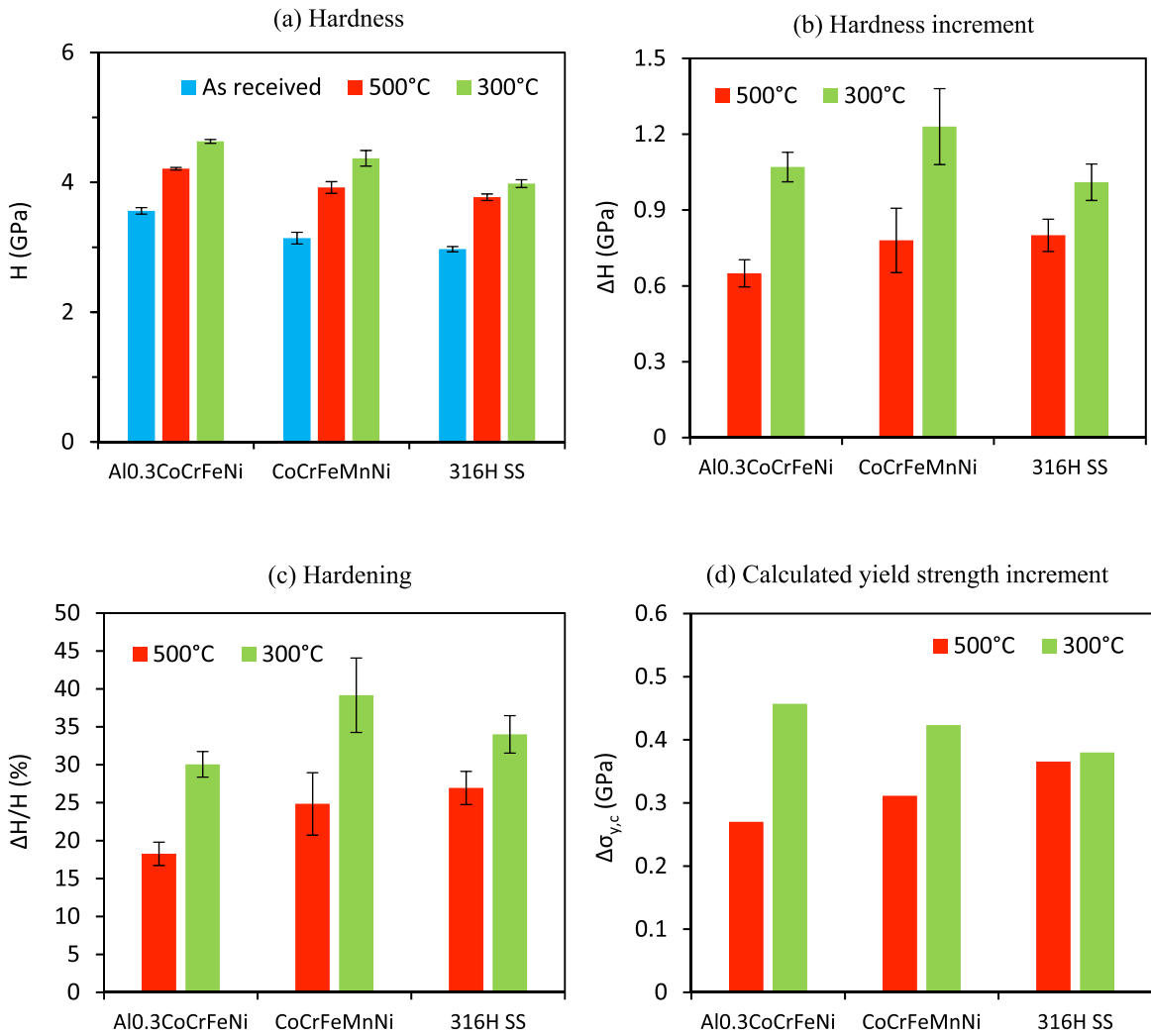


Fig. 9. (a) The hardness measured by nanoindentation for the as received and irradiated Al_{0.3}CoCrFeNi, CoCrFeMnNi and 316H SS to 1 dpa. The error bar is equal to one standard deviation. (b) The hardness increases of the three materials after irradiation to 1 dpa. (c) The relative hardness increases of the three materials after irradiation to 1 dpa. The error bar in (b) and (c) are uncertainty propagation calculated from the error bar in (a). (d) Calculated increase in yield strength using Orowan equation. The hardness for the as received and the samples irradiated at 300 °C was taken from Ref. [15].

phase at 550 °C, and likely also at 500 °C. In this study, the L₁₂ particles were only observed after irradiation, and were not present after the thermal annealing as shown in Fig. 2. This suggests that irradiation enhanced the kinetics of L₁₂ phase formation in Al_{0.3}CoCrFeNi significantly.

L₁₂ diffraction spots were observed in the Al_{0.3}CoCrFeNi after irradiation at both 300 °C and 500 °C. However, the intensity of the diffraction spots was significantly stronger at 500 °C than at 300 °C. Also, with much stronger diffraction spots, L₁₂ particles in dark field TEM images can be formed with L₁₂ {110} diffraction spots as shown in Fig. 3. Our previous experiment at 300 °C could not evidently find L₁₂ particles with the same imaging technique. Obviously, the 500 °C specimen had a higher volume fraction of L₁₂ phase with a better-defined domain as compared with the 300 °C specimen.

The difference in the observation of nanoparticles between 300 °C and 500 °C may be explained with the vacancy mobility and the transition from short-range order (SRO) to long-range order

(LRO). At 300 °C, vacancies in Al_{0.3}CoCrFeNi were not mobile enough to form LRO in the short irradiation time (~17 min). The weak ordering transformation at 300 °C may have proceeded in a continuous form of concentration wave [25], resulting in SRO. The SRO would not provide sufficient diffraction contrast for imaging. At 500 °C, on the other hand, vacancies were more mobile, making LRO possible through the nucleation and growth of L₁₂ nanoparticles. In addition, aluminum is a low-melting-point element (M.P. 659 °C). The aluminum may become quite mobile at 500 °C and promote the formation of Ni₃Al phase.

In contrast to the Al_{0.3}CoCrFeNi, no new phases were observed in the CoCrFeMnNi and 316H SS after irradiation at 500 °C and 300 °C to 1 dpa. The relatively lower phase stability of Al_{0.3}CoCrFeNi as compared with CoCrFeMnNi and 316H SS was due to the larger atomic mismatch and enthalpy of mixing. Using the solid solution criterion proposed by Yang and Zhang [26], the Al_{0.3}CoCrFeNi has a larger atomic mismatch (δ), indicating larger lattice distortion and strain, and a smaller ratio of mixing entropy and enthalpy (Ω),

indicating a higher tendency to decompose, as compared with the CoCrFeMnNi and 316H SS [15].

4.2. Morphology of defect clusters

While the size and density of dislocation loops were comparable between HEAs and 316H SS under irradiation at 300 °C [15], the loop size and density were strikingly different at 500 °C where HEAs exhibited much larger and less dense dislocation loops as compared with 316H SS. In addition, a stronger foil thickness dependence of microstructure was observed at 500 °C.

For all materials after irradiation at 500 °C to 1 dpa, we observed small “black-spot” defect clusters in the thin regions under about 100 nm. As the thickness increased, large dislocation loops began to appear, and their areal densities increased linearly with increasing thickness as shown in Fig. 6. Some small defect clusters remained visible in the thick regions. The large dislocation loops were believed to be interstitial type based on the studies on similar materials [7,10,27–29]. The small vacancy defect clusters were primarily SFT in the HEAs, and primarily dislocation loops in the 316H SS. The lack of SFT in the 316H SS was consistent with the previous observations on stainless steels [30,31]. As suggested by Zinkle and Sindelar [30], a low vacancy diffusivity or a distinct cascade collapse mechanism is responsible for the low population of SFT in stainless steels. The different SFT fraction between the HEAs and 316H SS implies that the vacancy diffusivity is lower in the 316H SS than in the HEAs. It is also possible that the collapse of cascades is noticeably different between the 316H SS and HEAs.

The variations of interstitial dislocation loops and vacancy clusters with the foil thickness indicate a sink effect of foil surfaces. At 500 °C, both interstitials and vacancies were mobile and could migrate to the surface. As a result, the concentrations of both vacancies and interstitials decreased in the studied materials close to the foil surface. However, since interstitials had a significantly higher mobility than vacancies, the surface-affected zone without interstitial loops would be thicker than the zone without vacancy-type defects. As the depth increased, the interstitial concentration increased, passing a threshold value of forming dislocation loops, and therefore large dislocation loops were observed. The depletion of interstitial loops near the foil surface in this study is consistent with a previous experiment on a Fe–Ni–Cr alloy irradiated with 1.5 MeV krypton ions and 1 MeV electrons at 450 °C where a denuded zone of 75 nm was observed [32].

On the other hand, the presence of vacancy clusters in the thin regions may be explained with two mechanisms. Firstly, the vacancies had a much smaller mobility as compared with interstitials. Therefore, the surface-affected zone for vacancy clusters was much shallower. As a result, there were still sufficient vacancies to form SFT or vacancy loops in the thin regions while large interstitial loops were absent. Actually, the imbalance between interstitials and vacancies can lead to a reduced chance of recombination, and enhance the survival of vacancies and the formation of vacancy clusters in the vicinity of foil surface [33,34]. Secondly, the vacancy clusters can be formed by cascade collapse. With a displacement cascade, atoms are replaced and transported to the outskirt of a melted region, resulting in a vacancy-rich core at the melt center. Vacancies can cluster shortly after cascade [35]. Once clustered, the mobility of vacancies would be further reduced, and their chance to be lost to the foil surface would be insignificant.

The observation of denuded zones of interstitial dislocation loops at foil surfaces leads to two inferences. Firstly, the depth of denuded zone was about 50 nm for all three materials, which indicates that the mobility of self-interstitials was not significantly different among these materials. This is reasonable since the capture radii of impurities for migrating interstitials decreases with

increasing temperature, and approaches zero at about 150 K as shown by Dworschak et al. [36]. At the irradiation temperature used in this study, the difference in interstitial mobility is negligibly small among different materials. Consequently, similar depletion profiles of interstitial loops were observed near foil surfaces in both HEAs and 316H SS.

As shown in Fig. 6, the density of interstitial dislocation loops decreases from the 316H SS to the CoCrFeMnNi and to the Al_{0.3}CoCrFeNi, while the loop size increases from one material to another following the same order. Nonetheless, our result shows that the HEAs have a lower loop density and larger loop size than the 316H SS. If the 316H SS can be considered as a “simpler” alloy as compared to HEAs, this is consistent with the finding by Shi et al. [12], where loop size was found increase, and density decrease, with increasing number of major alloying elements. In contrast, our result contradicts to the observations by Kumar et al. where a smaller loop size and larger loop density were found when a HEA of FeNiMnCr was compared with 316 SS [1], and also Lu et al. where HEAs exhibited smaller loop size and larger loop density as compared with simpler alloys and pure metals [5,6].

While both our study and Shi’s work [12] were performed with *in-situ* irradiations on thin foils, the studies by Kumar et al. and Lu et al. [1,6] were conducted with much thicker samples. One may argue that the conflicting observations were due to the surface sink effect. However, the average loop size observed in our thin foil samples is very similar to that observed in bulk samples. For example, in the studies by Williams [28,37], bulk samples of 316 SS irradiated with 46 MeV nickel ions at the same 500 °C to 1 dpa showed an average loop size between 7.7 and 10.1 nm, which is very close to our measurement of 9.9 nm in the 316H SS. Obviously, our results obtained from a thin-foil irradiation are not notably different from that obtained from “bulk” irradiation. This is understandable since once dislocation loops start to populate in the irradiated materials, they will become the dominant sinks, shielding the effect of foil surface.

It is evident that the surface effect is not a controlling factor for the observed differences in the loop size and density between the HEAs and 316H SS in this study. The nucleation and growth of dislocation loops depends on many variables such as the concentration of point defects, the mobility of defects, the binding of the defects to the clusters etc. In this study, the Al_{0.3}CoCrFeNi clearly exhibited the lowest nucleation rate, while the 316H SS exhibited the highest. It is possible that Al_{0.3}CoCrFeNi had a lower interstitial concentration that lead to a low nucleation rate of dislocation loops. However, provided that most interstitials were already in the loops, the calculated number of interstitials in loops per unit volume does not support this hypothesis. On the other hand, a higher activation barrier for loop nucleation may be the reason for having a lower nucleation rate in the Al_{0.3}CoCrFeNi. Following the treatment by Russell and Powell [38], the steady-state nucleation rate J_k is

$$J_k = Z' \beta_k \rho_k' \quad (2)$$

where Z' is the Zeldovich factor. β_k is rate of interstitial capture by a loop of critical size. ρ_k' is the equilibrium concentration of critical nuclei in classical nucleation theory, which in turn is given by

$$\dot{\rho}_k = \alpha N_0 e^{\left(\frac{-\Delta G_k'}{kT} \right)} \quad (3)$$

where N_0 is the interstitial sites per unit volume. α is the orientational factor. kT is Boltzmann constant times absolute temperature. $\Delta G_k'$ is the energy barrier for the nucleation of interstitial dislocation loops. It is the maximum of $\Delta G_n'$, which in turn is given by

$$\Delta G_n = kT \sum_0^{n-1} \ln \left[\frac{\beta_v(j+1)}{\beta_i(j)} + e^{\left(\frac{\delta G_f^o}{kT} \right)} \right] \quad (4)$$

where $\beta_v(j+1)$ is the rate of vacancy impingement on an interstitial loop of $j+1$ interstitials, and $\beta_i(j)$ is the rate of interstitial impingement on an interstitial loop of j interstitials. β_i and β_j are proportional to the diffusivities of interstitial and vacancy, respectively. δG_f^o is denoted as the difference in formation energy between interstitial loops with $j+1$ and j interstitials without the presence of vacancies. Based on this formalism, the higher the vacancy diffusivity, the larger the energy barrier for loop nucleation, and the lower the nucleation rate of dislocation loops. With regard to our results, the $\text{Al}_{0.3}\text{CoCrFeNi}$ should have the highest vacancy diffusivity, followed by the CoCrFeMnNi and then the 316H SS.

This vacancy diffusivity relationship is also consistent with the observation of SFT where the $\text{Al}_{0.3}\text{CoCrFeNi}$ had the largest and most well-defined SFT, while the 316H SS had a very small density of SFT. Although HEAs are generally considered to have lower diffusivities as compared with conventional alloys [39], the low vacancy diffusivity of the 316H SS is not entirely surprising. The high carbon content in 316H SS can significantly reduce its vacancy mobility due to a carbon-vacancy binding effect [40,41]. As a result, a decreasing void swelling rate with increasing carbon content had been observed in 316 SS at 500 to 600 °C [37,42,43]. In addition, as shown in Fig. 10, a parallel 1.25 MeV electron irradiation study using a high voltage electron microscope in Hokkaido University at 460–500 °C shows that the shape of dislocation loops in the 316H SS was crenulated, while the loops in the $\text{Al}_{0.3}\text{CoCrFeNi}$ and CoCrFeMnNi were round-shaped. The formation of the crenulated interstitial dislocation loops has been considered to be due to the effect of carbon on the vacancy flux toward the loop [44–46]. Note that perfect loops were observed in the 316H SS under the high-energy electron irradiation, which was different from the heavy-ion irradiation conducted in this study.

On the other hand, it is unclear why the CoCrFeMnNi would have a lower vacancy diffusivity than the $\text{Al}_{0.3}\text{CoCrFeNi}$. After all, they both had very low carbon concentrations, while the $\text{Al}_{0.3}\text{CoCrFeNi}$ had a larger lattice distortion and supposedly a lower vacancy diffusivity. It is likely that a higher oxygen content in the CoCrFeMnNi trapped vacancies and resulted in a lower vacancy diffusivity, which produces a similar effect to that of carbon in the 316H SS.

In summary, our results suggest that the vacancy mobility was the controlling mechanism for the observed variation in loop size and density among the studied HEAs and 316H SS. The observation

of SFT and crenulated dislocation loops also indicates a dominant role of vacancies in microstructural evolution in the HEAs and 316H SS. The effects of stacking fault energy, strain energy and the concentration of interstitials are not clear at present, and requires further investigations.

4.3. Irradiation hardening

As shown in Fig. 9(a), the unirradiated hardness measured by nanoindentation was the highest for the $\text{Al}_{0.3}\text{CoCrFeNi}$, followed by the CoCrFeMnNi and then 316H SS. The larger hardness value of the $\text{Al}_{0.3}\text{CoCrFeNi}$ can be attributed to its larger lattice distortion. The 316H SS was strengthened by carbon interstitials, but its hardness was still lower than the two HEAs. The indent size in this study was about 200 nm, which was substantially smaller than the grain sizes of all materials. Therefore, the measured values in this study were related to their intrinsic hardness, and were not affected by their grain sizes. On the other hand, because of the large grain size, the indents performed in this study were insufficient to show the effect of grain orientation. However, as shown by Miura et al. [47] and Liu et al. [48], the hardness variation due to grain orientation in ion-irradiated stainless steels was small as compared with the variation between different conditions of this study.

After irradiation at 500 °C to 1 dpa, although the ranking of the absolute hardness H in Fig. 9(a) remains the same ($\text{Al}_{0.3}\text{CoCrFeNi} > \text{CoCrFeMnNi} > 316\text{H SS}$), the relative hardening as shown in Fig. 9(b) and (c) reverses (316H SS > $\text{CoCrFeMnNi} > \text{Al}_{0.3}\text{CoCrFeNi}$). The HEAs show a lower level of irradiation hardening than the 316H SS at 500 °C. The lower degree of irradiation hardening of HEAs is a good sign for their applications in advanced nuclear reactors which will be operated at high temperatures (e.g. 400–600 °C for sodium fast reactor, 550–700 °C for molten salt reactor [16]). A consistent trend between ΔH in Fig. 9(b) and calculated $\Delta\sigma_{yc}$ in Fig. 9(d) has been observed in this study. This suggests that the decreases in ΔH in the HEAs were due to their lower dislocation loop densities, which in turn were due to their higher vacancy mobilities.

5. Conclusion

The $\text{Al}_{0.3}\text{CoCrFeNi}$, CoCrFeMnNi and 316H stainless steel had been irradiated with 1 MeV krypton ions at 500 °C to 1 dpa under *in-situ* TEM observation. The irradiation at 500 °C resulted in an ordered L1₂ phase transformation in the $\text{Al}_{0.3}\text{CoCrFeNi}$. No phase transformation was observed in the CoCrFeMnNi and 316H SS. The irradiation-induced defect clusters had been analyzed as a function of foil thickness, revealing the sink effect of foil surfaces. Within about 50 nm near the foil surfaces, a high-density of vacancy

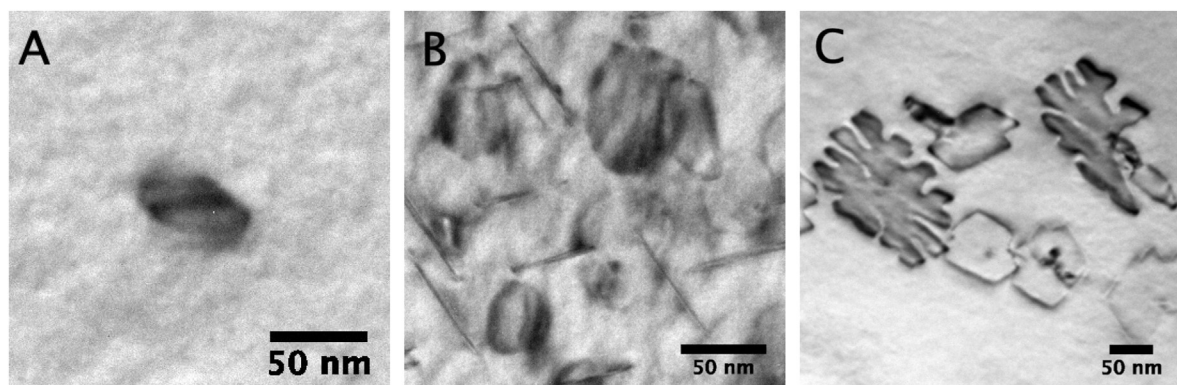


Fig. 10. The dislocation loops produced by 1.25 MeV electrons in (A) $\text{Al}_{0.3}\text{CoCrFeNi}$, (B) CoCrFeMnNi and (C) 316H SS at 460–500 °C to a unspecified dose.

clusters, i.e. SFT and loops, was observed. Beyond 50 nm, interstitial dislocation loops resolvable under TEM started to appear, and their size and density gradually saturated as foil thickness increased. For loop size, the Al_{0.3}CoCrFeNi has the largest, followed by the CoCr-FeMnNi and 316H SS. For loop density, the 316H SS has the largest, followed by the CoCrFeMnNi and Al_{0.3}CoCrFeNi. These rankings in loop size and density among the studied materials may be related to the differences in vacancy mobility. Among the three alloys, the 316H SS may have the lowest vacancy mobility due to its carbon content. A higher vacancy mobility reduced the nucleation rate, which in turn favored the growth of loops in the HEAs as compared with the 316H SS.

The nanoindentation results indicate that the irradiation hardening at 500 °C was less in the HEAs than in the 316H SS, consistent with the observation of the loop density. While more comprehensive investigations are still needed, the result of this study provides a promising sign for the applications of HEAs at high temperature nuclear reactors. This study also showed that the effect of interstitial impurities can have a profound impact on the radiation performance of complex alloys like austenitic SSs and HEAs.

CRediT authorship contribution statement

Wei-Ying Chen: Conceptualization, Data curation, Formal analysis, Funding acquisition, Investigation, Methodology, Writing - original draft, Project administration. **Marquis A. Kirk:** Investigation, Writing - review & editing. **Naoyuki Hashimoto:** Data curation, Investigation, Writing - review & editing. **Jien-Wei Yeh:** Resources, Writing - review & editing. **Xiang Liu:** Data curation, Writing - review & editing. **Yiren Chen:** Funding acquisition, Supervision, Writing - review & editing.

Declaration of competing interest

The authors declare that they have no known competing financial interests or personal relationships that could have appeared to influence the work reported in this paper.

Acknowledgements

The authors would like to thank Dr. Meimei Li (ANL) for her support and discussion on this study. Mr. Peter Baldo (ANL) is thanked for operating the ion accelerator. Dr. Yinbin Miao (ANL) and Dr. Christopher Ulmer (PSU) for the fruitful discussion. This work was supported by Laboratory Directed Research and Development funding from Argonne National Laboratory, provided by the Director, Office of Science, of the U.S. Department of Energy under Contract No. DE-AC02-06CH11357. The *in-situ* TEM experiment was supported by DOE, Office of Nuclear Energy, under DOE Idaho Operations Office Contract DE-AC07-05ID14517 as part of a Nuclear Science User Facilities. Nanoindentation was carried out at the Frederick Seitz Materials Research Laboratory, University of Illinois at Urbana-Champaign.

References

- [1] N.A.P.K. Kumar, C. Li, K.J. Leonard, H. Bei, S.J. Zinkle, Microstructural stability and mechanical behavior of FeNiMnCr high entropy alloy under ion irradiation, *Acta Mater.* 113 (2016) 230–244, <https://doi.org/10.1016/j.actamat.2016.05.007>.
- [2] D.J.M. King, S.T.Y. Cheung, S.A. Humphry-Baker, C. Parkin, A. Couet, M.B. Cortie, G.R. Lumpkin, S.C. Middleburgh, A.J. Knowles, High temperature, low neutron cross-section high-entropy alloys in the Nb-Ti-V-Zr system, *Acta Mater.* 166 (2019) 435–446, <https://doi.org/10.1016/j.actamat.2019.01.006>.
- [3] A. Kairee, J.C. Waite, B. Li, A. Couet, D.E.J. Armstrong, A.J. Wilkinson, Short communication: 'Low activation, refractory, high entropy alloys for nuclear applications', *J. Nucl. Mater.* 526 (2019) 151744, <https://doi.org/10.1016/j.jnucmat.2019.151744>.
- [4] C. Li, X. Hu, T. Yang, N.K. Kumar, B.D. Wirth, S.J. Zinkle, Neutron irradiation response of a Co-free high entropy alloy, *J. Nucl. Mater.* 527 (2019) 151838, <https://doi.org/10.1016/j.jnucmat.2019.151838>.
- [5] C. Lu, T. Yang, K. Jin, N. Gao, P. Xiu, Y. Zhang, F. Gao, H. Bei, W.J. Weber, K. Sun, Y. Dong, L. Wang, Radiation-induced segregation on defect clusters in single-phase concentrated solid-solution alloys, *Acta Mater.* 127 (2017) 98–107, <https://doi.org/10.1016/j.actamat.2017.01.019>.
- [6] C. Lu, L. Niu, N. Chen, K. Jin, T. Yang, P. Xiu, Y. Zhang, F. Gao, H. Bei, S. Shi, M.-R. He, I.M. Robertson, W.J. Weber, L. Wang, Enhancing radiation tolerance by controlling defect mobility and migration pathways in multicomponent single-phase alloys, *Nat. Commun.* 7 (2016) 13564, <https://doi.org/10.1038/ncomms13564>.
- [7] M.-R. He, S. Wang, K. Jin, H. Bei, K. Yasuda, S. Matsumura, K. Higashida, I.M. Robertson, Enhanced damage resistance and novel defect structure of CrFeCoNi under *in situ* electron irradiation, *Scripta Mater.* 125 (2016) 5–9, <https://doi.org/10.1016/j.scriptamat.2016.07.023>.
- [8] K. Jin, C. Lu, L.M. Wang, J. Qu, W.J. Weber, Y. Zhang, H. Bei, Effects of compositional complexity on the ion-irradiation induced swelling and hardening in Ni-containing equiatomic alloys, *Scripta Mater.* 119 (2016) 65–70, <https://doi.org/10.1016/j.scriptamat.2016.03.030>.
- [9] M. Sadeghilaridjani, A. Ayyagari, S. Muskeri, V. Hasannaeimi, R. Salloom, W.Y. Chen, S. Mukherjee, Ion irradiation response and mechanical behavior of reduced activity high entropy alloy, *J. Nucl. Mater.* 529 (2020) 151955, <https://doi.org/10.1016/j.jnucmat.2019.151955>.
- [10] T. Yang, W. Guo, J.D. Poplawsky, D. Li, L. Wang, Y. Li, W. Hu, M.L. Crespillo, Z. Yan, Y. Zhang, Y. Wang, S.J. Zinkle, Structural damage and phase stability of Al_{0.3}CoCrFeNi high entropy alloy under high temperature ion irradiation, *Acta Mater.* 188 (2020) 1–15, <https://doi.org/10.1016/j.actamat.2020.01.060>.
- [11] S.J. Zinkle, L.L. Snead, Designing radiation resistance in materials for fusion energy, *Annu. Rev. Mater. Res.* 44 (2014) 241–267, <https://doi.org/10.1146/annurev-matsci-070813-113627>.
- [12] S. Shi, M.R. He, K. Jin, H. Bei, I.M. Robertson, Evolution of ion damage at 773K in Ni-containing concentrated solid-solution alloys, *J. Nucl. Mater.* 501 (2018) 132–142, <https://doi.org/10.1016/j.jnucmat.2018.01.015>.
- [13] M.-R. He, S. Wang, S. Shi, K. Jin, H. Bei, K. Yasuda, S. Matsumura, K. Higashida, I.M. Robertson, Mechanisms of radiation-induced segregation in CrFeCoNi-based single-phase concentrated solid solution alloys, *Acta Mater.* 126 (2017) 182–193, <https://doi.org/10.1016/j.actamat.2016.12.046>.
- [14] Y. Zhang, G.M. Stocks, K. Jin, C. Lu, H. Bei, B.C. Sales, L. Wang, L.K. Béland, R.E. Stoller, G.D. Samolyuk, M. Caro, A. Caro, W.J. Weber, Influence of chemical disorder on energy dissipation and defect evolution in concentrated solid solution alloys, *Nat. Commun.* 6 (2015) 8736, <https://doi.org/10.1038/ncomms9736>.
- [15] W.-Y. Chen, X. Liu, Y. Chen, J.-W. Yeh, K.-K. Tseng, K. Natesan, Irradiation effects in high entropy alloys and 316H stainless steel at 300 °C, *J. Nucl. Mater.* 510 (2018) 421–430, <https://doi.org/10.1016/j.jnucmat.2018.08.031>.
- [16] S.J. Zinkle, J.T. Busby, Structural materials for fission & fusion energy, *Mater. Today* 12 (2009) 12–19, [https://doi.org/10.1016/S1369-7021\(09\)70294-9](https://doi.org/10.1016/S1369-7021(09)70294-9).
- [17] J.-W. Yeh, Alloy design strategies and future trends in high-entropy alloys, *JOM* 65 (2013) 1759–1771, <https://doi.org/10.1007/s11837-013-0761-6>.
- [18] R.E. Stoller, M.B. Toloczo, G.S. Was, A.G. Certain, S. Dwaraknath, F.A. Garner, On the use of SRIM for computing radiation damage exposure, *Nucl. Instrum. Methods Phys. Res. Sect. B Beam Interact. Mater. Atoms* 310 (2013) 75–80, <https://doi.org/10.1016/J.NIMB.2013.05.008>.
- [19] M. Li, M.A. Kirk, P.M. Baldo, D. Xu, B.D. Wirth, Study of defect evolution by TEM with *in situ* ion irradiation and coordinated modeling, *Philos. Mag.* 92 (2012) 2048–2078, <https://doi.org/10.1080/14786435.2012.662601>.
- [20] P. Hosemann, D. Kiener, Y. Wang, S.A. Maloy, Issues to consider using nano indentation on shallow ion beam irradiated materials, in: *J. Nucl. Mater.*, North-Holland, 2012, pp. 136–139, <https://doi.org/10.1016/j.jnucmat.2011.11.070>.
- [21] C.-J. Tong, Y.-L. Chen, J.-W. Yeh, S.-J. Lin, S.-K. Chen, T.-T. Shun, C.-H. Tsau, S.-Y. Chang, Microstructure characterization of Al x CoCrCuFeNi high-entropy alloy system with multiprincipal elements, *Metall. Mater. Trans. A* 36 (2005) 881–893, <https://doi.org/10.1007/s11661-005-0283-0>.
- [22] S. Zinkle, Y. Matsukawa, Observation and analysis of defect cluster production and interactions with dislocations, *J. Nucl. Mater.* 329–333 (2004) 88–96, <https://doi.org/10.1016/j.jnucmat.2004.04.298>.
- [23] T.-T. Shun, Y.-C. Du, Microstructure and tensile behaviors of FCC Al0.3CoCrFeNi high entropy alloy, *J. Alloys Compd.* 479 (2009) 157–160, <https://doi.org/10.1016/j.jallcom.2008.12.088>.
- [24] B. Gwalani, V. Soni, D. Choudhuri, M. Lee, J.Y. Hwang, S.J. Nam, H. Ryu, S.H. Hong, R. Banerjee, Stability of ordered L12 and B2 precipitates in face centered cubic based high entropy alloys – Al0.3CoFeCrNi and Al0.3CuFeCrNi2, *Scripta Mater.* 123 (2016) 130–134, <https://doi.org/10.1016/j.scriptamat.2016.06.019>.
- [25] S. Banerjee, K. Urban, M. Wilkens, Order-disorder transformation in Ni4Mo under electron irradiation in a high-voltage electron microscope, *Acta Metall.* 32 (1984) 299–311, [https://doi.org/10.1016/0001-6160\(84\)90103-2](https://doi.org/10.1016/0001-6160(84)90103-2).
- [26] X. Yang, Y. Zhang, Prediction of high-entropy stabilized solid-solution in multi-component alloys, *Mater. Chem. Phys.* 132 (2012) 233–238, <https://doi.org/10.1016/j.matchemphys.2011.11.021>.
- [27] S.J. Zinkle, P.J. Maziasz, R.E. Stoller, Dose dependence of the microstructural evolution in neutron-irradiated austenitic stainless steel, *J. Nucl. Mater.* 206 (1993) 266–286, [https://doi.org/10.1016/0022-3115\(93\)90128-L](https://doi.org/10.1016/0022-3115(93)90128-L).
- [28] T.M. Williams, Interstitial loop nucleation and growth in solution-treated type

- 316 stainless steel irradiated to low doses with 22 MeV C²⁺ and 46.5 MeV Ni⁶⁺ ions, *J. Nucl. Mater.* 79 (1979) 28–42, [https://doi.org/10.1016/0022-3115\(79\)90431-8](https://doi.org/10.1016/0022-3115(79)90431-8).
- [29] C. Lu, T. Yang, L. Niu, Q. Peng, K. Jin, M.L. Crespillo, G. Velisa, H. Xue, F. Zhang, P. Xiu, Y. Zhang, F. Gao, H. Bei, W.J. Weber, L. Wang, Interstitial migration behavior and defect evolution in ion irradiated pure nickel and Ni-xFe binary alloys, *J. Nucl. Mater.* 509 (2018) 237–244, <https://doi.org/10.1016/J.JNUCMAT.2018.07.006>.
- [30] S.J. Zinkle, R.L. Sindelar, Defect microstructures in neutron-irradiated copper and stainless steel, *J. Nucl. Mater.* 155–157 (1988) 1196–1200, [https://doi.org/10.1016/0022-3115\(88\)90495-3](https://doi.org/10.1016/0022-3115(88)90495-3).
- [31] A. Rowcliffe, R. Nicholson, Quenching defects and precipitation in a phosphorus-containing austenitic stainless steel, *Acta Metall.* 20 (1972) 143–155, [https://doi.org/10.1016/0001-6160\(72\)90122-8](https://doi.org/10.1016/0001-6160(72)90122-8).
- [32] T. Kimoto, C.W. Allen, L.E. Rehn, Growth rate of dislocation loop in Fe-Ni-Cr alloy under Kr⁺ ion and electron irradiation, *J. Nucl. Mater.* 191–194 (1992) 1194–1197, [https://doi.org/10.1016/0022-3115\(92\)90663-6](https://doi.org/10.1016/0022-3115(92)90663-6).
- [33] M.J. Aliaga, R. Schäublin, J.F. Löffler, M.J. Caturla, Surface-induced vacancy loops and damage dispersion in irradiated Fe thin films, *Acta Mater.* 101 (2015) 22–30, <https://doi.org/10.1016/J.ACTAMAT.2015.08.063>.
- [34] S.J. Zinkle, L.L. Snead, Opportunities and limitations for ion beams in radiation effects studies: bridging critical gaps between charged particle and neutron irradiations, *Scripta Mater.* 143 (2018) 154–160, <https://doi.org/10.1016/J.JSCRIPTAMAT.2017.06.041>.
- [35] T.D. de la Rubia, R.S. Averback, R. Benedek, W.E. King, Role of thermal spikes in energetic displacement cascades, *Phys. Rev. Lett.* 59 (1987) 1930–1933, <https://doi.org/10.1103/PhysRevLett.59.1930>.
- [36] F. Dworschak, R. Lennartz, H. Wollenberger, Interstitial trapping and detrappling in electron irradiated dilute copper alloys, *J. Phys. F Met. Phys.* 5 (1975) 400–418, <https://doi.org/10.1088/0305-4608/5/3/004>.
- [37] T.M. Williams, The effect of soluble carbon on void swelling and low dose dislocation structures in type 316 austenitic stainless steel irradiated with 46.5 MeV Ni⁶⁺ ions, *J. Nucl. Mater.* 88 (1980) 217–225, [https://doi.org/10.1016/0022-3115\(80\)90277-9](https://doi.org/10.1016/0022-3115(80)90277-9).
- [38] K. Russell, R. Powell, Dislocation loop nucleation in irradiated metals, *Acta Metall.* 21 (1973) 187–193, [https://doi.org/10.1016/0001-6160\(73\)90002-3](https://doi.org/10.1016/0001-6160(73)90002-3).
- [39] K.-Y. Tsai, M.-H. Tsai, J.-W. Yeh, Sluggish diffusion in Co–Cr–Fe–Mn–Ni high-entropy alloys, *Acta Mater.* 61 (2013) 4887–4897, <https://doi.org/10.1016/J.ACTAMAT.2013.04.058>.
- [40] J.A. Slane, C. Wolverton, R. Gibala, Experimental and theoretical evidence for carbon-vacancy binding in austenite, *Metall. Mater. Trans. A* 35 (2004) 2239–2245, <https://doi.org/10.1007/s11661-006-0203-y>.
- [41] J.A. Slane, C. Wolverton, R. Gibala, Carbon–vacancy interactions in austenitic alloys, *Mater. Sci. Eng. A* 370 (2004) 67–72, <https://doi.org/10.1016/J.JMSEA.2003.08.073>.
- [42] M.J. Makin, G.P. Walters, A.J.E. Foreman, The void swelling behaviour of electron irradiated type 316 austenitic steel, *J. Nucl. Mater.* 95 (1980) 155–170, [https://doi.org/10.1016/0022-3115\(80\)90090-2](https://doi.org/10.1016/0022-3115(80)90090-2).
- [43] N. Igata, Y. Kohno, N. Tanabe, F. Rotman, H. Tsunakawa, Effects of nitrogen and carbon on void swelling in austenitic stainless steels, *J. Nucl. Mater.* 122 (1984) 219–223, [https://doi.org/10.1016/0022-3115\(84\)90599-3](https://doi.org/10.1016/0022-3115(84)90599-3).
- [44] F.A. Garner, D.S. Gelles, Irradiation creep mechanisms: an experimental perspective, *J. Nucl. Mater.* 159 (1988) 286–309, [https://doi.org/10.1016/0022-3115\(88\)90098-0](https://doi.org/10.1016/0022-3115(88)90098-0).
- [45] E.H. Lee, N.H. Packan, M.B. Lewis, L.K. Mansur, Effects of rapidly pulsed ion bombardment on microstructure and phase stability in a Ti-modified stainless steel, *Nucl. Instrum. Methods Phys. Res. Sect. B Beam Interact. Mater. Atoms* 16 (1986) 251–259, [https://doi.org/10.1016/0168-583X\(86\)90021-2](https://doi.org/10.1016/0168-583X(86)90021-2).
- [46] A. Hishinuma, Y. Katano, K. Fukaya, K. Shiraiishi, Radiation damage in stainless steel electron irradiated in a high voltage electron microscope, *J. Nucl. Sci. Technol.* 13 (1976) 656–662, <https://doi.org/10.3327/jinst.13.656>.
- [47] T. Miura, K. Fujii, K. Fukuya, K. Takashima, Influence of crystal orientation on hardness and nanoindentation deformation in ion-irradiated stainless steels, in: *J. Nucl. Mater.*, North-Holland, 2011, pp. 984–987, <https://doi.org/10.1016/j.jnucmat.2010.12.197>.
- [48] X. Liu, J.G. Gigax, J.D. Poplawsky, W. Guo, H. Kim, L. Shao, F.A. Garner, J.F. Stubbins, Radiation response of a Fe–20Cr–25Ni austenitic stainless steel under Fe²⁺ irradiation at 500 °C, *Materialia* 9 (2020) 100542, <https://doi.org/10.1016/J.MTLA.2019.100542>.